

Visible and Terahertz Nonlinear Responses in the Topological Noble Metal Dichalcogenide PdTe₂

George J. de Coster,^{1, 2, *} Lucas Lafeta,^{3, †} Stefan Heiserer,¹ Cormac Ó Coileáin,¹ Zdenek Sofer,⁴ Achim Hartschuh,³ Georg S. Duesberg,¹ and Paul Seifert^{1, ‡}

¹*Institute of Physics, University of the Bundeswehr Munich,
Faculty of Electrical Engineering and Information Technology,
Werner-Heisenberg-Weg. 39, 85577 Neubiberg, Germany*

²*DEVCOM Army Research Laboratory, 2800 Powder Mill Road, Adelphi, MD, 20738 USA*

³*Department of Chemistry and Center for NanoScience (CeNS),
Ludwig-Maximilians-Universität München, Butenandtstraße 5-13 (E), 81377 Munich, Germany*

⁴*Department of Inorganic Chemistry, University of Chemistry and
Technology Prague, Technická 5, 166 28 Prague 6, Czech Republic*

(Dated: November 18, 2025)

Nonlinear processes can offer pathways to next-generation sensors and frequency mixing devices to overcome modern imaging, detection, and communication challenges. In this article, we report on strong second and third-order nonlinear optical responses in visible and terahertz (THz) light in single crystals of the noble metal dichalcogenide PdTe₂. We find that buried conduction and valence topological surface states of PdTe₂ lead to resonant enhancement of optical second-harmonic generation. On the other hand, although the nonlinear responses obtained with THz excitation are not close to this resonance, they can be clearly observed in reflection geometry, even in the presence of broadband excitation, where optical filters are not necessary to observe the odd-order higher harmonic gain. By carefully considering the radiative photocurrent framework of stimulated THz emission, we are able to extract fingerprints of both second- and third-order processes in the THz regime, and show that PdTe₂ is a promising material candidate for radio frequency rectification, frequency mixing, and beam focusing.

I. INTRODUCTION

Quantum materials with strong spin-orbit coupling and topological surface states have spawned new device concepts that exploit nonlinear optical (NLO) rectification and higher-harmonic generation [1–4], the Josephson diode effect [5, 6], and spin-orbit torque switching [7, 8]. NLO responses in quantum materials are particularly relevant to polarization sensitive imaging, frequency conversion, and radio frequency (RF) detection, as even inversion symmetric crystal systems can exhibit strong second-harmonic generation (SHG), polarization dependent photocurrent generation, and rectification-processes classically forbidden by symmetry [1, 9–12]. Such effects often originate from topological surface states, which enable broadband photocurrent and DC rectification spanning near-UV to THz frequencies [10, 13–15].

Layered noble metal dichalcogenides (NMDs), (Pd, Pt)(Te,Se,S)₂, have recently been recognized as a distinctive class of 2D quantum materials, which combine metallic conductivity, strong spin-orbit coupling, and topologically nontrivial electronic structures. They crystallize predominantly in the centrosymmetric 1T phase (space group P3m1) with octahedral coordination of the transition metal (Fig. 1(a) and (b)), and have recently

been shown to be accessible via low-temperature synthesis methods [16, 17]. Among them, PdTe₂ is a type-II Dirac semimetal which hosts both topological surface states and superconductivity [18, 19]. Related compounds such as PtTe₂ and PtSe₂ exhibit non-saturating magnetoresistance, high carrier mobilities, and thickness-driven band-structure evolution from semimetallic to semiconducting behavior [20–26]. Despite their inversion symmetry, NMDs display unexpectedly strong NLO effects, including SHG, shift currents, and photogalvanic responses, attributed to local symmetry breaking, surface and interface fields, or strain-induced distortions [27–31]. Their large second-order susceptibilities are enhanced by spin-orbit coupling and Berry curvature effects, making them promising candidates for tunable NLO devices. Their 2D nature allows straightforward integration into MEMS architectures and tuning via thickness control, Janus engineering, or strain [2, 32–36].

In this work, we verified the crystalline quality and symmetry of the PdTe₂ flakes using Raman spectroscopy (Fig. 1(c) and (d)), showing the characteristic E_g and A_{1g} phonon modes, and by lattice-resolution atomic force microscopy (AFM) imaging (Fig. 1(e)), revealing the expected hexagonal surface lattice (0.39 nm lattice constant). A representative bulk crystal is shown in Fig. 1(c), and the schematic band structure (Fig. 1(f)) illustrates the type-II Dirac dispersion with topological surface states and surface-projected Dirac cones.

Moreover, we demonstrate NLO and harmonic generation in PdTe₂ in both the visible (\sim 1.5 eV) and terahertz range (\sim 0.1–3 THz), revealing persistent and tun-

* george.j.decoster.civ@army.mil

† lucas.lafeta@cup.lmu.de

‡ paul.seifert@unibw.de

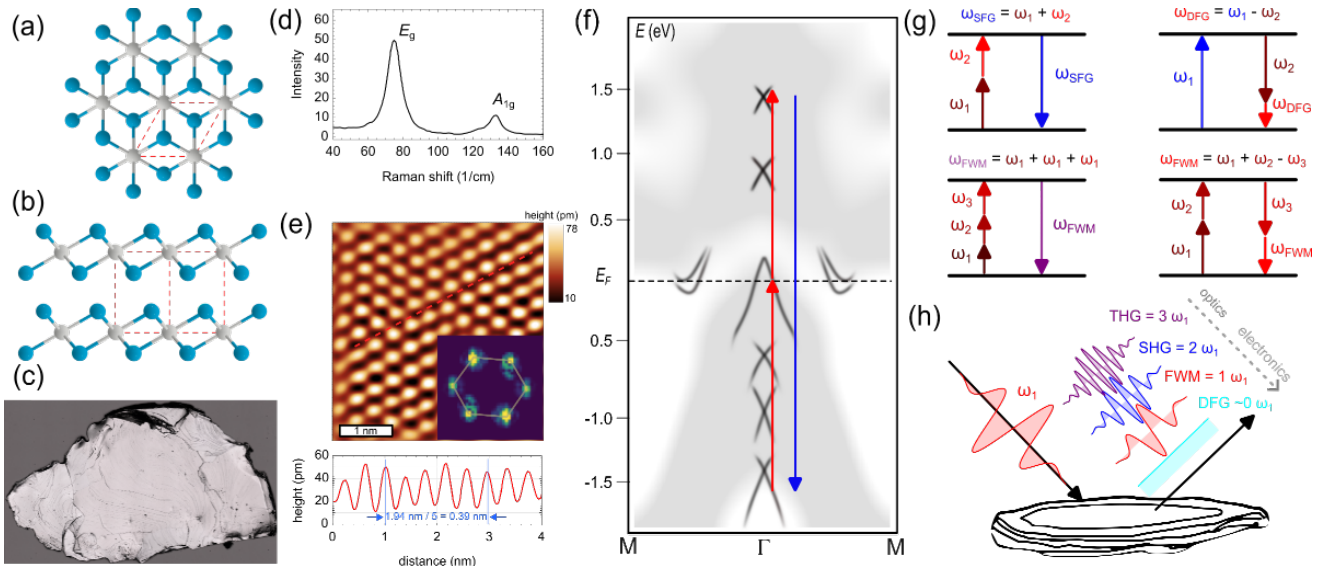


FIG. 1. (a) Top view and (b) side view of 1T layered crystal structure of PdTe₂ with Pd atoms shown in gray and Se atoms shown in blue. (c) Optical microscopy image of a ~ 5 mm bulk layered PdTe₂ crystal. (d) Raman spectrum of PdTe₂. (e) Lattice-resolution AFM image (Fourier-filtered), with profile along the red dashed line (below). Inset, fast Fourier transform of the AFM image. (f) Schematic electronic structure of PdTe₂ along the Γ – M direction with bulk bands indicated in gray and surface (projected) bands and topological surface states indicated in black. A possible resonant condition for SHG is shown by the arrows (red-excitation, blue-emission). (g) Generic second- and third-order sum-frequency generation (SFG), second-order difference-frequency generation (DFG), and third-order FWM processes, highlighting the energy exchange between interacting photons. (h) Schematic illustration of SHG, THG, FWM and DFG processes from a near monochromatic wave packet.

able nonlinear responses in this centrosymmetric topological semimetal. These responses at disparate optical bands invite a closer examination of the nonlinear mechanisms that can arise in layered systems such as PdTe₂. We outline the fundamental principles of NLO interactions in 2D materials, emphasizing how local symmetry breaking and spin-orbit-driven band topology can enhance their nonlinear susceptibilities.

II. PRINCIPLES OF NONLINEAR OPTICS IN 2D MATERIALS

NLO techniques have become essential tools for probing 2D materials. SHG, a second-order process, is widely used to determine lattice orientation and symmetry in noncentrosymmetric systems such as hBN and transition metal dichalcogenides [37–39], while third-order techniques like four-wave mixing (FWM) probe resonant transitions and excitonic responses [40]. The optical response of a medium arises from the induced polarization $\mathbf{P}(\mathbf{r}, t)$ caused by the incident electric field $\mathbf{E}(\mathbf{r}, t)$:

$$\mathbf{P} = \varepsilon_0 \left(\chi^{(1)} \mathbf{E} + \chi^{(2)} \mathbf{E}^2 + \chi^{(3)} \mathbf{E}^3 + \dots \right), \quad (1)$$

where $\chi^{(n)}$ is the n th-order susceptibility tensor. At low field intensities, the linear term ($\chi^{(1)}$) dominates, whereas higher intensities activate nonlinear terms. The tensor rank grows with order ($\chi^{(1)}$: 9 elements, $\chi^{(2)}$: 27,

$\chi^{(3)}$: 81), and the nonvanishing elements are dictated by crystal symmetry [41]. Even-order processes vanish in perfectly centrosymmetric materials ($\chi^{(2n)} = 0$), implying that SHG and related effects arise only when inversion symmetry is locally broken. In frequency space the second-order nonlinear polarization responsible for SHG is given by:

$$\mathbf{P}^{(2)}(2\omega_1) = \varepsilon_0 \chi^{(2)} \mathbf{E}(\omega_1) \mathbf{E}(\omega_1), \quad (2)$$

which corresponds to the second order sum frequency process in Fig. 1(g) with $\omega_1 = \omega_2$. The third-order term corresponding to FWM is:

$$\mathbf{P}^{(3)}(2\omega_1 - \omega_3) = \varepsilon_0 \chi^{(3)} \mathbf{E}(\omega_1) \mathbf{E}(\omega_1) \mathbf{E}^*(\omega_3). \quad (3)$$

This particular degenerate case of third order corresponds to the bottom third order optical process in Fig. 1(g) with $\omega_1 = \omega_2$. It gives rise to sum and difference degenerated FWM [41]. The spectral dependence of the nonlinear response tensors are discussed in Sections III and IV. We note here that enhancements to SHG and FWM are anticipated when the excitation pathways or emission correspond to resonances within the bandstructure [40], as indicated by the resonant SHG process at 2.95 eV in Fig. 1(f).

The form and symmetries of $\chi^{(2)}$ and $\chi^{(3)}$ are easily computed using the C_{3v} surface point group of 1T-PdTe₂. These results are well known and not shown here [42–44]. When bulk inversion symmetry is further imposed on the

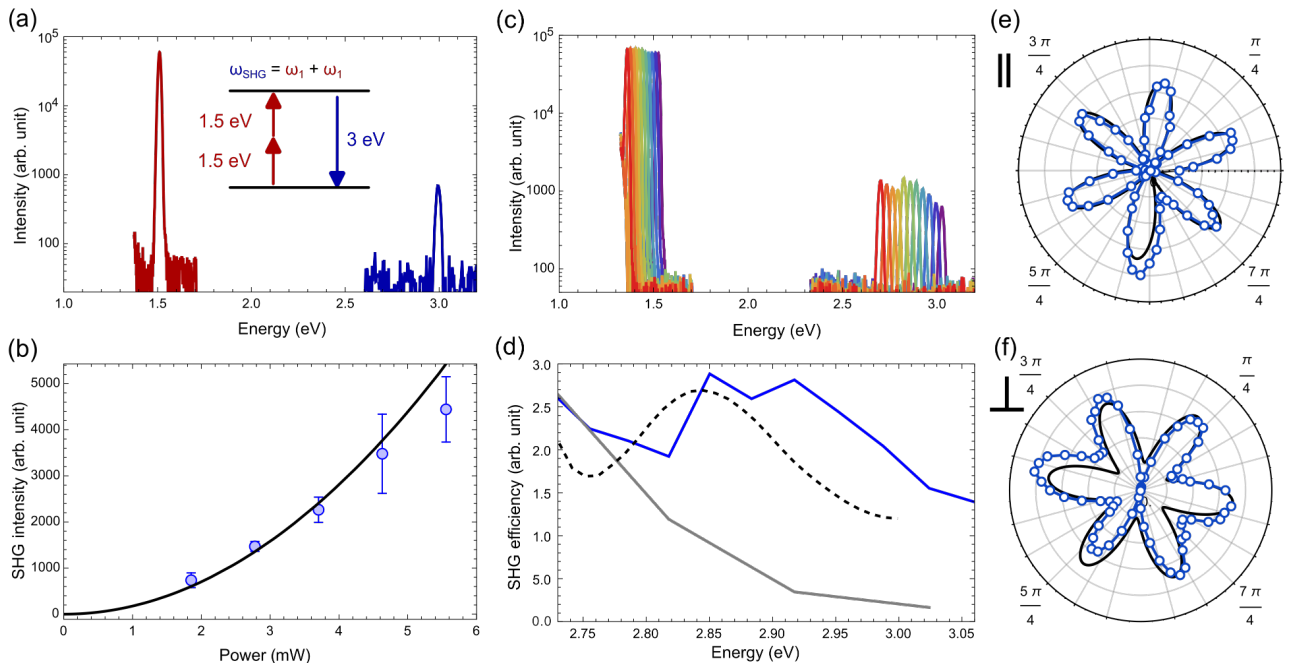


FIG. 2. (a) Optical second harmonic generation at 3 eV in PdTe₂ stimulated by a 1.5 eV pulsed laser. (b) The power dependence of the SHG at 3 eV is shown to be quadratic in the pulse power, consistent with SHG scaling. The input pulse wavelength is varied in (c) and the resulting normalized SHG efficiency is plotted in (d) in blue. The experimental blue curve resembles the overlayed J DOS calculation (black dashed line) for PdTe₂ based on the band structure in Fig. 1(f), with a resonance near 2.95 eV, which is the separation of the highest and lowest energy Dirac points in PdTe₂. The gray curve is the SHG intensity of the bright spots shown by the SHG scan of Fig. 7 in the Appendix, showing they are likely defects without additional optical resonances in this excitation band. The symmetry of the parallel (e) and cross (f) polarization of the SHG response to varying the polarization of the 1.5 eV pulse by a half-wave plate synchronous with a polarizer in front of the detector is checked and found to exhibit six-fold symmetry consistent with the C_{3v} surface point group of PdTe₂.

tensors, $\chi^{(2)}$ becomes trivially zero. In centrosymmetric materials like PdTe₂, strong spin-orbit coupling, surface states, and strain fields can locally break inversion symmetry and amplify Berry curvature effects, resulting in finite $\chi^{(2)}$ and enhanced $\chi^{(3)}$. These mechanisms provide a natural explanation for the broadband nonlinear and harmonic generation responses observed experimentally.

III. NONLINEAR OPTICAL RESPONSES TO VISIBLE LIGHT IN PDTE₂

A. Second Harmonic Generation

The emission of SHG in the noble metal dichalcogenides was investigated previously [30, 45, 46]. Despite the inversion symmetry of the point group D_{3d} (P3m1 space group) for the 1T phase (see Figs. 1(a) and (b)), experiments have seen non-zero emission of SHG by the surface of PdTe₂, governed by the C_{3v} point group symmetries of the surface [46]. In our studies, we focus the experiments on the PdTe₂ sample shown in Fig. 1(c). To probe second harmonic generation, we excite the PdTe₂ with a pulsed 1.5 eV (~825 nm) laser, generating a second-order signal at 3 eV (~412.5 nm). Figure 2(a) shows the

observed spectra of the emission of the SHG in blue and the residual incident field after the short-pass in red.

The quadratic power dependence of the SHG intensity is shown in Fig. 2(b) using the same condition as measured in Fig. 2(a). This quadratic behavior is characteristic of the second-order process which corroborates the second harmonic generation process in the PdTe₂. Figure 2(c) next presents the spectra of SHG using various wavelengths, the region at 1.5 eV shows the incident field after shortpass filtering. The peaks close by 3 eV are the SHG by the respective incident wavelength. We can compute the SHG intensity as the ratio of output intensity at 2 ω to the square of the input intensity at ω once we have the proportion $I_{SHG} \propto I_{input}^2$ and present this in Fig. 2(d). We find that the SHG intensity peaks between 2.8 and 2.95 eV (Fig. 2(d) solid blue line) follows the computed joint density of states (J DOS) of PdTe₂ (Fig. 2(d) dashed line). The phenomenological agreement between J DOS and SHG intensity and resonance near 2.9 eV demonstrates that the SHG is enhanced when resonant with real level transitions [40], and likely corresponds to the optical process identified in the band structure plot of Fig. 1(f). The gray curve in Fig. 2(d) is the second-harmonic generated by bright spots in the sample, probably caused by defects (see Appendix A), which are

smaller than the spot size diameter of the laser ($\sim 1 \mu\text{m}$). The SHG of the bright spots presents a different polarization dependence compared with the PdTe₂ surface (Fig. 7(h)) and the SHG spectrum does not present resonance, showing a monotonic spectrum, potentially caused by the optical setup and detection, used as a reference point to compare features in the PdTe₂ surface spectrum.

Figures 2(e) and (f) respectively show the experimental polar dependency of the SHG signal upon rotating the incident electric field synchronously with the polarizer in the detection parallel and perpendicular, respectively. The six-fold rotational symmetry of the polarization intensity is the signature of an underlying three-fold rotation symmetric lattice. The data is closely fit by the functional form (black) expected for surface C_{3v} point group symmetry [42, 43]. The defects, on the other hand, possess a generic two-fold rotational symmetry of their SHG spectrum (see Appendix A) which follows from many point groups and thus only serves to show the defects break the symmetry of the parent lattice.

B. Four-Wave Mixing

We next investigated the third-order nonlinear regime using FWM, which, unlike second-order processes, does not rely on symmetry breaking and is allowed in all media. FWM provides direct access to the third-order susceptibility $\chi^{(3)}$, offering insight into the intrinsic electronic nonlinearity of PdTe₂. Special cases such as third harmonic generation (THG) and degenerate FWM (DFWM) have been widely used to probe materials, including h-BN, graphene, carbon nano tubes, and TMDs [47–52]. We demonstrate a DFWM process in bulk PdTe₂ samples. Figure 3(a) shows the FWM spectrum generated by two degenerate pump fields at 1.59 eV ($\sim 780 \text{ nm}$) and one probe at 1.33 eV ($\sim 932 \text{ nm}$), producing a fourth wave at 1.86 eV ($\sim 667 \text{ nm}$). Fig. 3(b) presents the power dependence of the FWM signal which follow the the proportion $I_{\text{FWM}} \propto I_{\text{pump}}^2 I_{\text{probe}}$. When the pump power is fixed at $\sim 1.1 \text{ mW}$ and the probe power is varied, the FWM intensity shows linear scaling with I_{probe} (red curve). Inversely, by fixing the probe power at $\sim 1.1 \text{ mW}$ and varying the pump power, the FWM intensity then scales as I_{probe}^2 (orange curve). The FWM intensity scaling can be calculated from the combination of these two measurements, and results in a cubic scaling with total input power (green curve).

We further probed the symmetries of the FWM signal by subjecting both pump and probe incident laser to half-wave plate rotations by synchronously rotating a polarizer in front of the detector, and then collecting the resulting signal at parallel and cross polarizations to the incident beams. The results in Figs. 3(c) and (d) show near-uniform behavior as a function of wave-plate angle, with almost no signal present in the cross polarization detection. This is consistent with the symmetry of PdTe₂ for third-order processes. The slight deviations

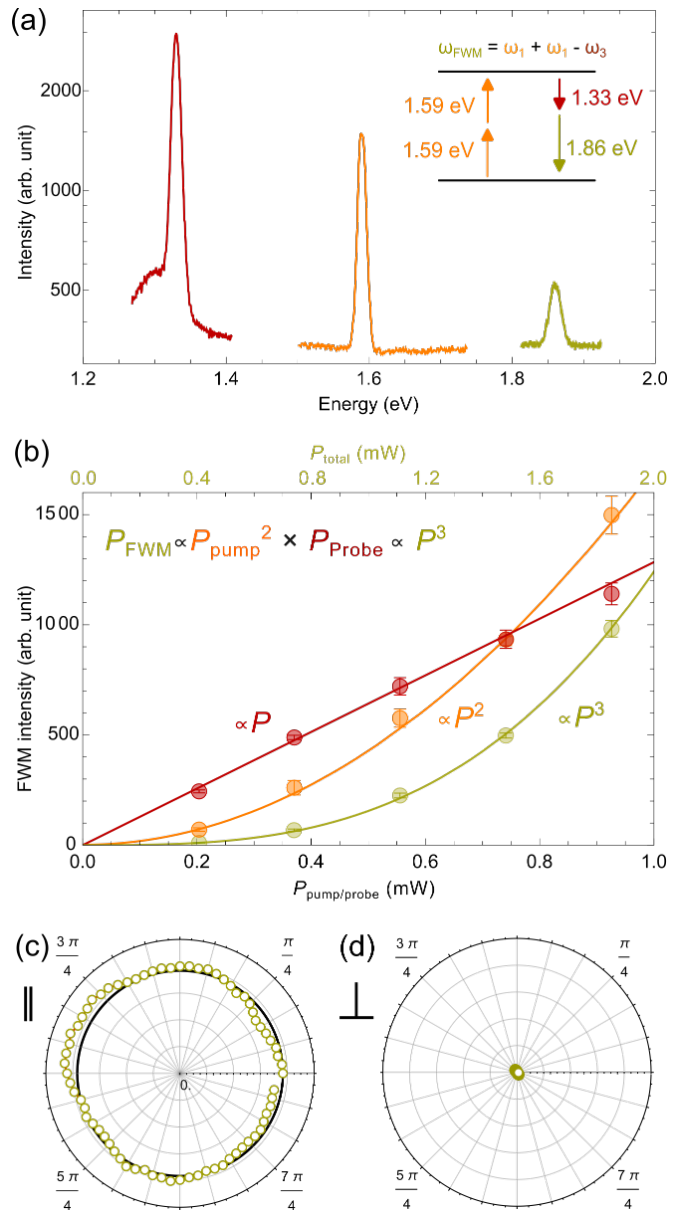


FIG. 3. (a) Visible optical FWM probing of the third-order nonlinear response of PdTe₂ is conducted using 1.59 eV and 1.33 eV pump and probe pulses, respectively. (b) The power dependence of the FWM intensity is found to be quadratic in pump intensity and linear in probe intensity, yielding an overall cubic intensity dependence, consistent with a four-wave mixing effect. The input and output fields are again subjected to half-wave plate rotation of their polarization, and the symmetry of the parallel (c) and cross (d) polarization detected fields was probed. Consistent with C_{3v} surface point group symmetry, there is effectively no third-order response at cross polarization, and circular symmetry for the parallel detection.

from uniformity in Fig. 3(c) can be attributed to the optical setup efficiency in certain polarization directions and alignment of the wave-plate with the polarizer in the

detection.

The observation of a strong DFWM signal in PdTe₂ reveals a clear third-order nonlinear susceptibility. The response likely arises from resonant contributions of Dirac-like interband transitions and surface electronic states, which can enhance $\chi^{(3)}$ even in metallic systems [53–58]. This highlights PdTe₂ as a promising platform for broadband nonlinear photonics extending beyond the semiconducting 2D material family.

IV. THZ SPECTROSCOPY

By investigating the response of PdTe₂ to THz radiation, we can determine if the NLO activity of interband transitions probed by SHG and FWM disappears for smaller, intraband energy scales (1 THz corresponds to 4.14 meV). Similarly to our experiments at optical frequencies, we performed THz time-domain spectroscopy on the PdTe₂ in atmosphere under reflection geometry using a pulse centered around ~ 0.7 THz. The reflected pulse was sampled in time, and a pulse reflected off a gold mirror was used as a reference signal to determine the spectrum of the excitation pulse.

The time-domain signal of a reference pulse and the THz pulse generated by reflecting off the PdTe₂ crystal surface are shown in Fig. 4(a). In Fig. 4(b) we show the spectrum of these two pulses where clear dips corresponding to absorption by atmospheric water vapor can be seen. We observe that while the total power reflected by the PdTe₂ is lower than for the reference pulse, for particular frequency bands, $f < 0.2$ THz and $1.5 < f < 2.7$ THz, the spectral intensity emitted by PdTe₂ is higher than the spectral intensity of the reference pulse. This is a clear indication of nonlinear optical activity that enhances the output at these frequencies. In particular, the low-frequency, near-DC, behavior can only arise from frequency-difference processes in an even-order nonlinear response, such as optical rectification or photogalvanic or photon drag effects, since the excitation pulse does not have spectral contributions at such low frequencies [10, 44]. Given the broad bandwidth of our excitation pulse, however, multiple higher harmonic generation (HHG) orders could conceivably contribute to the observed gain, since the individual contributions cannot be clearly separated as in the visible NLO experiments.

To determine which HHG orders are present within the PdTe₂ spectrum, we performed a power dependence study. Using a pair of polarizers placed after the THz emitter, we vary the orientation of the first while keeping the second fixed. As a result, we can fit the spectrum $E_{rad}(f)$ as a function of the power P for each frequency f . The injected and emitted electric fields, $E_{in}(f)$ and $E_{rad}(f)$, are complex. By assuming $|E_{in}(f)| = \mathcal{E}_0 \sqrt{P}$ for some frequency independent constant \mathcal{E}_0 we can derive a fitting equation for the real valued spectrum as a function

of power $|E_{rad}(f, P)|^2$:

$$|E_{rad}(f, P)|^2 = |\chi^{(1)}(f)P^{1/2} + \chi^{(2)}(f)P + \chi^{(3)}(f)P^{3/2}|^2. \quad (4)$$

We have now absorbed powers of \mathcal{E}_0 into $\chi^{(n)}$. The power dependence and corresponding fits at the pulse center frequency, as well as its multiples and in the low frequency limit, are shown in Fig. 5(a). The linear response, SHG, and THG coefficients $|\chi^{(n=1,2,3)}(f)|$ are shown in Fig. 5(b). We note that although quadratic and cubic terms are mathematically independent, over the limited available power range with dominant linear response they become nearly collinear. Consequently, the fit converges to the dominant higher-order term rather than distributing weight across both.

From this analysis, we can conclude that the spectral gain observed at higher frequencies in Fig. 4c is due to THG, and the low-frequency excess is indeed due to a second-order process. Moreover, there is a strong third-order fundamental enhancement at the THz spectral peak, indicating that for high enough powers or narrow enough THz pulses, PdTe₂ could be used for pulse refocusing. We note that while we can distinguish the SHG of the bare PdTe₂ surface from the one generated by symmetry-breaking defects and edges etc in visible experiments, the large spot size diameter of 300 μm -500 μm in THz experiments makes these contributions indistinguishable. However, we believe the overall SHG intensity to be dominated by the bigger area of bare PdTe₂ surface.

We can compare the power analysis to the theoretically predicted HHG spectrum for the incoming pulse. The energy scales of THz spectroscopy (1 THz ~ 4 meV) are far below the interband transitions we studied with visible excitations, and the technique is often employed to probe Fermi surface or intraband contributions to the Drude conductivity in quantum materials [59]. At these energy and time scales, it is more natural to dynamically relate the radiated, $E_{rad}(t)$, and incoming, $E_{in}(t)$, electric fields through the photocurrent $j(t)$ generated by the NLO conductivity. In Appendix B, we show this can be written as:

$$j(t) = [\sigma^{(1)} * E_{in} + \sigma^{(2)} * E_{in}^2 + \sigma^{(3)} * E_{in}^3](t), \\ E_{rad}(t) \propto -\partial_t j(t; E_{in}(t)), \quad (5)$$

where $*$ is the convolution operator, and $\sigma^{(n)}(t_1, \dots, t_n)$ are the time dependent n th order nonlinear conductivities. Following our derivation in Appendix B, if the nonlinear response kernel $\sigma^{(n)}(\omega_1, \dots, \omega_n)$ is constant over the incoming spectrum $E_{in}(\omega)$ then the n th nonlinear contribution to the radiated spectrum, $E_{rad}^{(n)}(t)$ is simply

$$E_{rad}^{(n)}(t) \approx -\sigma_0^{(n)} E_{in}(t)^{n-1} \cdot \partial_t E_{in}(t). \quad (6)$$

Here $\sigma_0^{(n)}$ is the n th order NLO susceptibility strength, and we have suppressed the tensor nature of the NLO response, as for linearly polarized light, all components of

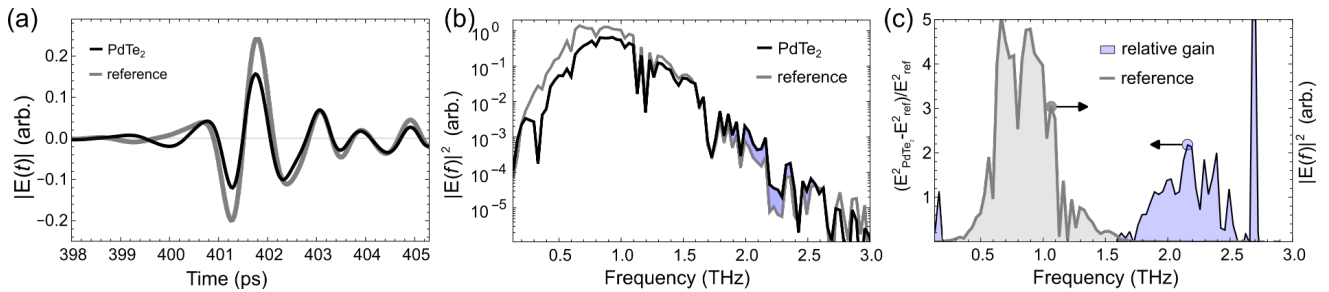


FIG. 4. (a) Time scans of the reference injected THz pulse and that emitted by PdTe₂ after illumination. The pulses are overlaid to show their qualitative difference. Their intensity Fourier spectra in (b) show the PdTe₂ emission is greater than the reference for some higher and lower frequencies. (c) Excitation spectrum (gray) and relative spectral gain in the reflected pulse (blue)

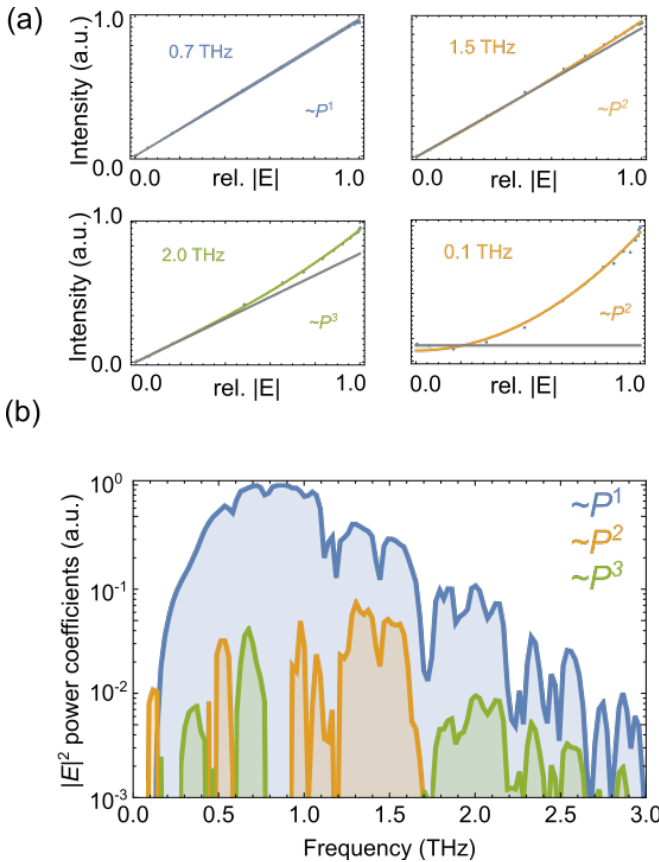


FIG. 5. (a) Power analysis of PdTe₂ THz emission spectrum intensity according to Eq. (4) shows mixing of quadratic, linear, and cubic behavior at different frequencies. For almost all frequencies, linear dominates except towards zero frequency, where quadratic takes over. (b) A log plot of the coefficients of Eq. (4) shows the fitting finds either linear plus quadratic or linear plus cubic behavior at a given frequency. Linear and cubic contributions are found to dominate the 1.7 THz to 2.7 THz band where PdTe₂ emits greater intensities than the reference pulse, suggesting third order processes are responsible for the observed gain.

$E_{in}(t)$ are in phase. Using Eq. (6) we calculate the theoretical second and third order emitted fields and present their Fourier spectra alongside $E_{in}(f)$ in Fig. 5. The theoretical spectrum indicates second and third order activity should be dominant for the same frequencies as determined by the power analysis in Fig. 5. However the theory in Fig. 6 predicts a SHG peak at ~ 1.75 eV while the power analysis instead displays a peak closer to ~ 1.5 eV. This can be accounted for by the atmospheric (mostly water) absorption in the laboratory. The reference pulse can be seen to have a large absorption peak around 1.75 eV. To verify this, we perform direct measurement of our THz pulse in free space and then in a box with purged nitrogen atmosphere maintaining the same path length as our reflection geometry experiments to obtain the transmission spectrum of our lab. We can then apply this transmission spectrum to the theoretical higher order response, and see that the atmospherically adjusted theoretical second order spectrum now peaks at ~ 1.5 eV in Fig. 6(a).

To obtain a greater understanding of the underlying excitation processes of the experimental observations, physically realistic nonlinear conductivity kernels have to be employed in the theoretical analysis. For example, in Appendix C we demonstrate that by properly employing the Drude conductivity for the linear response component we see that the *reflected* and incoming pulses are spectrally similar, and in fact become identical in the clean (i.e. long scattering time) limit. In the case of second order response, we seek to elucidate why the peak values of the DC and SHG contributions to E_{rad} are comparable. The true $\sigma^{(2)}(\omega_1, \omega_2)$ function will not be spectrally flat due to resonant transitions and excitation lifetimes. Consider the second-order shift and injection current response functions introduced by Braun *et al.* [60]:

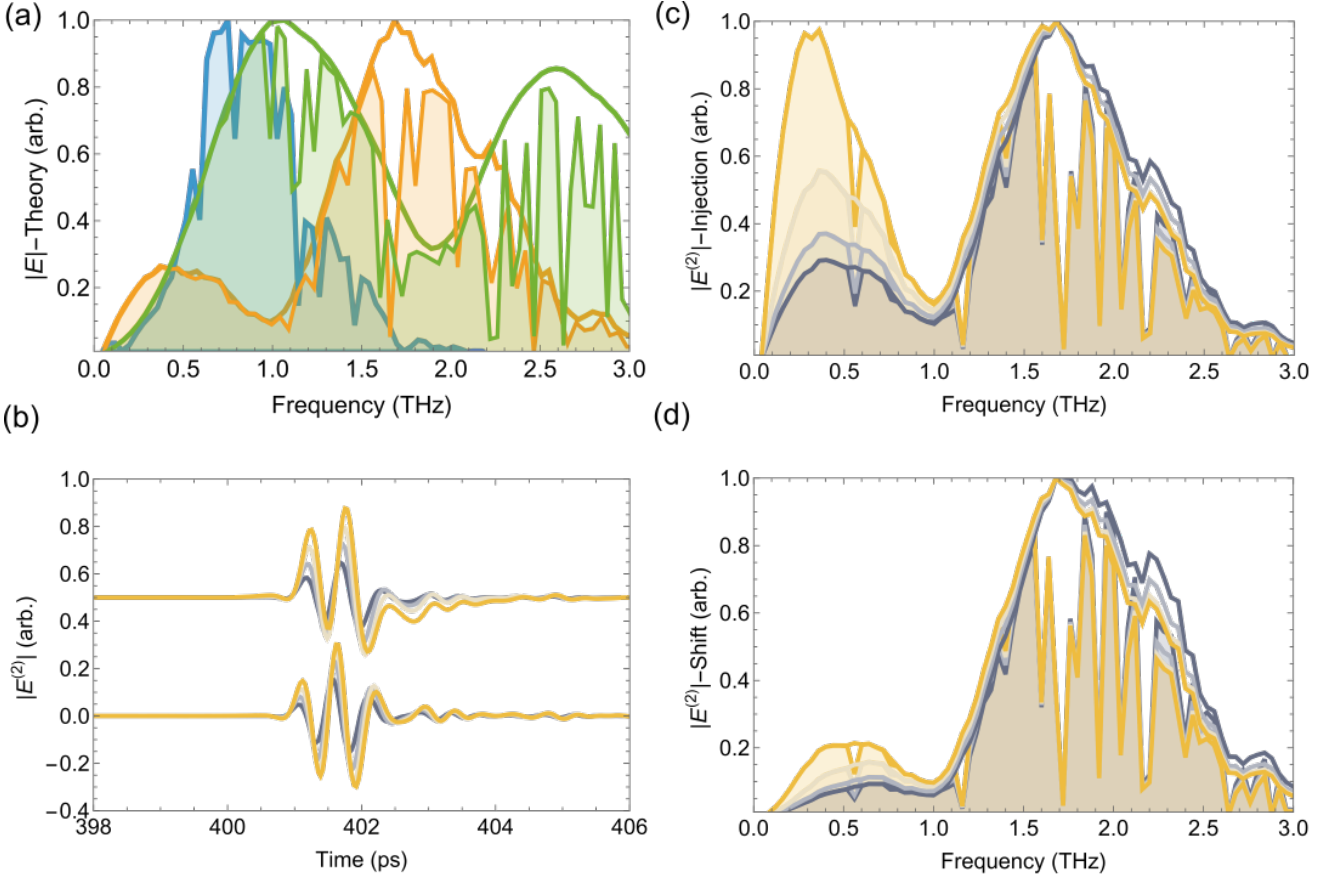


FIG. 6. (a) Second (orange) and third (green) order response spectra calculated according to Eq. (6) using the reference THz pulse (blue). Each spectrum is individually normalized by its peak intensity. The filled curves show the result of applying laboratory transmission and absorption to the theoretical spectra. (b) Time-dependent radiated pulses generated by injection (top) and shift (bottom) currents for increasing lifetimes $\tau_{inj/sh} = 0.05, 0.1, 0.2, 0.5$ ps are shown in the gray to yellow colored curves. The increasing lifetimes drive up the near DC response of the injection current. The corresponding Fourier spectra normalized by their peak intensity are shown in (c) and (d), where the filled curves account for atmospheric absorption and transmission. Phenomenologically, the injection current spectra for τ_{inj} more closely matches the data in Fig. 5.

$$\sigma_{inj}^{(2)}(t - t_1, t - t_2) = \sigma_{inj} \delta(t_1 - t_2) \Theta(t - t_1) e^{-(t-t_1)/\tau_{inj}}, \quad (7)$$

$$\sigma_{sh}^{(2)}(t - t_1, t - t_2) = \sigma_{sh} \delta(t_1 - t_2) \left(\delta(t - t_2) - \Theta(t - t_1) \frac{e^{-(t-t_1)/\tau_{sh}}}{\tau_{sh}} \right). \quad (8)$$

In this approximation, only the intensity of the electric field $|E(t)|^2$ matters due to the delta-function constraint $t_1 = t_2$. The relaxation times and strengths of the injection and shift excitations are given respectively by $\tau_{inj/sh}$ and $\sigma_{inj/sh}$. We apply these kernels to our injected THz pulse and take the time derivative to generate the emitted pulses in Fig. 6(b). We consider relaxation times of $\tau_{inj/sh} = 0.05, 0.1, 0.2$ and 0.5 ps to cover the orders of excitation timescales observable in THz spectroscopy [60]. The longer lifetimes translate into longer-lived second-order pulses, and correspondingly increase the weight of the near DC peak in the corresponding Fourier

spectra in Figs. 6(c) and (d). In the limit of a long shift current lifetime, $\tau_{sh} \rightarrow \infty$, the shift current response kernel approaches $\sigma_{sh}^{(2)}(t - t_1, t - t_2) \rightarrow \delta(t - t_1) \delta(t - t_2)$, which is equivalent to the simple theory approach discussed previously. This explains why the shift current and simple theory spectra in Figs. 6 (a) and (d) appear similar for long lifetimes. On the other hand, the injection current is dominated by the low frequency/DC response as the lifetime increases, suggesting that the second-order activity extracted in Fig. 5(b) originates from an injection current process with a lifetime on the order of 100 fs.

V. CONCLUSION

We have studied the NLO responses of single crystal PdTe₂ using visible (SHG and FWM) and THz spectroscopy. We conclude that second and third harmonic processes are clearly present in these disparate bands, indicating broadband nonlinear activity in PdTe₂ despite its inversion symmetric crystal structure.

In the visible studies we found the NLO response adheres to the surface point group symmetry C_{3v} of PdTe₂, which is consistent with the single crystal nature of the material. Moreover, despite the inversion symmetry of the bulk crystal, clear SHG was observed and was resonantly enhanced when the SHG energy coincided with the separation of topological surface state Dirac points. Such an enhancement between buried conduction and valence band Dirac points has previously been witnessed in topological insulator photogalvanic effect studies, and suggests PdTe₂ hosts a circular photogalvanic effect measurable in future studies [13].

In the THz spectroscopy studies, we found that linear response combined with third harmonic generation is sufficiently strong to produce a gain in the emitted spectrum at higher frequencies. Given that third harmonic generation is the sister process of fundamental enhancement, this suggests that PdTe₂ could be used for self-focusing and frequency upconversion in future THz-based studies. By studying the power dependence of our radiated spectrum, we were further able to extract both second and third order NLO processes, despite the broadband nature of the excitation pulse. Leveraging data on the transmission spectrum of our laboratory and careful application of nonlinear photocurrent theory, we found we could phenomenologically reproduce the experimental results using only the measured input pulse. To the best of our knowledge, the extraction of NLO activity in open atmosphere reflection geometry experiments is rarely conducted due to the challenges we overcame in this study. Our work lays the foundation for future THz reflection geometry experiments where transmission is not feasible, and provides a framework for studying NLO activity in broad spectra. Finally, the presence of SHG and near DC THz peaks in the emitted spectra shows that PdTe₂

likely possesses decent low-energy photogalvanic or photon drag effects. This motivates future studies on photocurrent generation in PdTe₂ to identify THz nonlinear photocurrent generation and possible nonlinear Hall effects. Particularly, the dependence of the photocurrent on the helicity of the incoming optical excitation controlled through a quarter-wave plate could clarify the injection versus shift current nature of the low-frequency second-order response.

ACKNOWLEDGMENTS

The authors thank Elisabeth Schreiner and Bärbel Zimmermann for performing the ToF-SIMS measurements of the PtSe₂ crystal. GJdC would like to acknowledge funding from the US Office of the Deputy Assistant Secretary of the Army for Defense Exports and Cooperation Engineering and Scientist Exchange Fellowship program. LL and AH were funded by the Deutsche Forschungsgemeinschaft (DFG, German Research Foundation) - 558231736. Z.S. was supported by ERC-CZ program (project LL2101) from Ministry of Education Youth and Sports (MEYS) and by the project Advanced Functional Nanorobots (reg. No. CZ.02.1.01/0.0/0.0/15_003/0000444 financed by the EFRR). This research was supported by a Laboratory University Collaborative Initiative award provided by the Basic Research Office in the Office of the Under Secretary of Defense for Research and Engineering and by the Army Research Office and was accomplished under Cooperative Agreement Number W911NF2520010 (STEP-TWO). The views and conclusions contained in this document are those of the authors and should not be interpreted as representing the official policies, either expressed or implied, of the Army Research Office or the U.S. Government. The U.S. Government is authorized to reproduce and distribute reprints for Government purposes notwithstanding any copyright notation herein. We thank dtac.bw—Digitalization and Technology Research Center of the Bundeswehr for support (project VITAL-SENSE). dtac.bw is funded via the German Recovery and Resilience Plan by the European Union (NextGenerationEU)

[1] J. Orenstein, J. Moore, T. Morimoto, D. Torchinsky, J. Harter, and D. Hsieh, *Annual Review of Condensed Matter Physics* **12**, 247 (2021).

[2] J. Shi, H. Xu, C. Heide, C. HuangFu, C. Xia, F. de Quesada, H. Shen, T. Zhang, L. Yu, A. Johnson, F. Liu, E. Shi, L. Jiao, T. Heinz, S. Ghimire, J. Li, J. Kong, Y. Guo, and A. M. Lindenberg, *Nature Communications* **14**, 10.1038/s41467-023-40373-z (2023).

[3] I. Sodemann and L. Fu, *Physical Review Letters* **115**, 10.1103/physrevlett.115.216806 (2015).

[4] Y. Onishi and L. Fu, *Phys. Rev. B* **110**, 075122 (2024).

[5] H. Wu, Y. Wang, Y. Xu, P. K. Sivakumar, C. Pasco, U. Filippozzi, S. S. P. Parkin, Y.-J. Zeng, T. McQueen, and M. N. Ali, *Nature* **604**, 653–656 (2022).

[6] P. K. Sivakumar, M. T. Ahari, J.-K. Kim, Y. Wu, A. Dixit, G. J. de Coster, A. K. Pandeya, M. J. Gilbert, and S. S. P. Parkin, *Communications Physics* **7**, 10.1038/s42005-024-01825-0 (2024).

[7] Y. Liu and Q. Shao, *ACS Nano* **14**, 9389–9407 (2020).

[8] J. Hidding, K. Mertiri, F. Mujid, C. Liang, J. Park, and M. H. D. Guimaraes, *Physical Review B* **108**, 10.1103/physrevb.108.064419 (2023).

[9] B. C. Connelly, P. J. Taylor, and G. J. de Coster, Proceedings of the National Academy of Sciences **121**, 10.1073/pnas.2307425121 (2024).

[10] H. Plank, J. Pernul, S. Gebert, S. N. Danilov, J. König-Otto, S. Winnerl, M. Lanius, J. Kampmeier, G. Musssler, I. Aguilera, D. Grützmacher, and S. D. Ganichev, Physical Review Materials **2**, 10.1103/physrevmateri-als.2.024202 (2018).

[11] Y.-M. Xie and N. Nagaosa, Proceedings of the National Academy of Sciences **122**, 10.1073/pnas.2424294122 (2025).

[12] M. Hemmat, S. Ayari, M. Mičica, H. Vergnet, S. Guo, M. Arfaoui, X. Yu, D. Vala, A. Wright, K. Postava, J. Mangeney, F. Carosella, S. Jaziri, Q. J. Wang, Z. Liu, J. Tignon, R. Ferreira, E. Baudin, and S. Dhillon, Info-
Mat **5**, 10.1002/inf2.12468 (2023).

[13] Y. Pan, Q.-Z. Wang, A. L. Yeats, T. Pillsbury, T. C. Flanagan, A. Richardella, H. Zhang, D. D. Awschalom, C.-X. Liu, and N. Samarth, Nature Communications **8**, 10.1038/s41467-017-00711-4 (2017).

[14] F. Hu, P. Zhao, L. Yang, S. Zhao, J. Lei, W. Li, J. Lai, Z. Yu, H. Park, C. Wong, R. Sharma, G. Eda, S. A. Yang, X. Xu, F. Wang, and H. Yang, Nature Nanotechnology 10.1038/s41565-025-01993-2 (2025).

[15] Y. Zhang and L. Fu, Proceedings of the National Academy of Sciences **118**, 10.1073/pnas.2100736118 (2021).

[16] C. Yim, K. Lee, N. McEvoy, M. O'Brien, S. Riazimehr, N. C. Berner, C. P. Cullen, J. Kotakoski, J. C. Meyer, M. C. Lemme, and G. S. Duesberg, ACS Nano **10**, 9550–9558 (2016).

[17] J. B. Mc Manus, D. V. Horvath, M. P. Browne, C. P. Cullen, G. Cunningham, T. Hallam, K. Zhussupbekov, D. Mullarkey, C. Ó Coileáin, I. V. Shvets, M. Pumera, G. S. Duesberg, and N. McEvoy, Nanotechnology **31**, 375601 (2020).

[18] W. Zheng, R. Schönenmann, N. Aryal, Q. Zhou, D. Rhodes, Y.-C. Chiu, K.-W. Chen, E. Kampert, T. Förster, T. J. Martin, G. T. McCandless, J. Y. Chan, E. Manousakis, and L. Balicas, Phys. Rev. B **97**, 235154 (2018).

[19] O. J. Clark, M. J. Neat, K. Okawa, L. Bawden, I. Marković, F. Mazzola, J. Feng, V. Sunko, J. M. Riley, W. Meevasana, J. Fujii, I. Vobornik, T. K. Kim, M. Hoesch, T. Sasagawa, P. Wahl, M. S. Bahramy, and P. D. C. King, Phys. Rev. Lett. **120**, 156401 (2018).

[20] M. N. Ali, L. M. Schoop, and et al., Scientific Reports **8**, 15383 (2018).

[21] P. Das, R. V. Chopdekar, and et al., Scientific Reports **6**, 31554 (2016).

[22] K. Zhussupbekov, L. Ansari, J. B. McManus, A. Zhussupbekova, I. V. Shvets, G. S. Duesberg, P. K. Hurley, F. Gity, C. Coileáin, and N. McEvoy, npj 2D Materials and Applications **5**, 10.1038/s41699-020-00196-8 (2021).

[23] W. Zheng, R. Schönenmann, N. Aryal, Q. Zhou, D. Rhodes, Y.-C. Chiu, K.-W. Chen, E. Kampert, T. Förster, T. J. Martin, G. T. McCandless, J. Y. Chan, E. Manousakis, and L. Balicas, arXiv (2018), reports large, non-saturating MR and mobilities $\sim 10^3$ – 10^4 cm²V⁻¹s⁻¹, 1805.00087.

[24] L. Zhao, Y. Wang, and et al., Physical Review Letters **124**, 036402 (2020).

[25] Q. Gao, H.-P. Komsa, A. V. Krasheninnikov, and et al., ACS Nano **15**, 12968 (2021).

[26] Z. Huang, K. Zhang, and et al., Materials Today Physics **11**, 100161 (2019).

[27] S. M. Faizanuddin, C.-H. Chien, Y.-J. Chan, S.-T. Liu, C.-N. Kuo, C. S. Lue, and Y.-C. Wen, Surface second harmonic generation from topological dirac semimetal pdte₂ (2023).

[28] G. Wang, K. Wang, N. McEvoy, Z. Bai, C. P. Cullen, C. N. Murphy, J. B. McManus, J. J. Magan, C. M. Smith, G. S. Duesberg, I. Kaminer, J. Wang, and W. J. Blau, Small **15**, 10.1002/smll.201902728 (2019).

[29] H. Wang, C. Zhang, and F. Rana, Nano Letters **15**, 8204–8210 (2015).

[30] L. Chu, Z. Li, H. Zhu, H. Lv, and F. Chen, Nanophotonics **13**, 3457 (2024).

[31] C. Guo, Y. Hu, G. Chen, D. Wei, L. Zhang, Z. Chen, W. Guo, H. Xu, C.-N. Kuo, C. S. Lue, X. Bo, X. Wan, L. Wang, A. Politano, X. Chen, and W. Lu, Science Advances **6**, eabb6500 (2020), <https://www.science.org/doi/pdf/10.1126/sciadv.abb6500>.

[32] C. Yim, V. Passi, M. C. Lemme, G. S. Duesberg, C. Ó Coileáin, E. Pallecchi, D. Fadil, and N. McEvoy, npj 2D Materials and Applications **2**, 10.1038/s41699-018-0051-9 (2018).

[33] Z. Peng, X. Chen, Y. Fan, D. J. Srolovitz, and D. Lei, Light: Science and Applications **9**, 10.1038/s41377-020-00421-5 (2020).

[34] X. Ge, X. Zhou, D. Sun, and X. Chen, ACS Omega **8**, 5715–5721 (2023).

[35] M. Cai, J. Zhang, Y. Chen, L. Hong, J. Fu, X. Zheng, Y. Yao, S. Zhang, Y. Liu, B. Dong, S. Chen, P. Li, G. You, J. Zhang, X. Guo, Y. Zhu, and S. Zhuang, Science Advances **11**, 10.1126/sciadv.adv0768 (2025).

[36] S. Heiserer, N. Galfe, M. Loibl, M. Wagner, O. Hartwig, S. Schlosser, S. Boche, W. Thornley, N. Clark, K. Lee, T. Stimpel-Lindner, C. Ó Coileáin, J. Kiendl, S. J. Haigh, G. J. de Coster, G. S. Duesberg, and P. Seifert, Advanced Materials 10.1002/adma.202412564 (2025).

[37] L. M. Malard, T. V. Alencar, A. P. M. Barboza, K. F. Mak, and A. M. de Paula, Phys. Rev. B **87**, 201401 (2013).

[38] Y. Li, Y. Rao, K. F. Mak, Y. You, S. Wang, C. R. Dean, and T. F. Heinz, Nano Lett. **13**, 3329 (2013).

[39] L. Lafeta, S. Hartmann, B. Rosa, S. Reitzenstein, L. M. Malard, and A. Hartschuh, ACS Photonics **12**, 357 (2025).

[40] L. Lafeta, A. Corradi, T. Zhang, E. Kahn, I. Bilgin, B. R. Carvalho, S. Kar, M. Terrones, and L. M. Malard, 2D Materials **8**, 35010 (2021).

[41] R. W. Boyd, in *Nonlinear Optics (Third Edition)*, edited by R. W. Boyd (Academic Press, Burlington, 2008) pp. 1–67.

[42] D. Hsieh, J. W. McIver, D. H. Torchinsky, D. R. Gardner, Y. S. Lee, and N. Gedik, Physical Review Letters **106**, 10.1103/physrevlett.106.057401 (2011).

[43] J. W. McIver, D. Hsieh, S. G. Drapcho, D. H. Torchinsky, D. R. Gardner, Y. S. Lee, and N. Gedik, Physical Review B **86**, 10.1103/physrevb.86.035327 (2012).

[44] Y. R. Shen, *The principles of nonlinear optics* (J. Wiley, New York, 1984).

[45] J. Yu, X. Kuang, J. Li, J. Zhong, C. Zeng, L. Cao, Z. Liu, Z. Zeng, Z. Luo, T. He, A. Pan, and Y. Liu, Nature Communications **12**, 10.1038/s41467-021-21267-4 (2021).

[46] S. M. Faizanuddin, C.-H. Chien, Y.-J. Chan, S.-T. Liu,

C.-N. Kuo, C. S. Lue, and Y.-C. Wen, Surface second harmonic generation from topological dirac semimetal pdte2 (2024), arXiv:2308.09053 [cond-mat.mtrl-sci].

[47] A. Virga, C. Ferrante, G. Batignani, D. De Fazio, A. D. G. Nunn, A. C. Ferrari, G. Cerullo, and T. Scopigno, *Nature Communications* **10**, 10.1038/s41467-019-11165-1 (2019).

[48] G. Gordeev, L. Lafeta, B. S. Flavel, A. Jorio, and L. M. Malard, *The Journal of Physical Chemistry C* **127**, 20438 (2023), <https://doi.org/10.1021/acs.jpcc.3c05696>.

[49] L. Lafeta, A. R. Cadore, T. G. Mendes-de Sa, K. Watanabe, T. Taniguchi, L. C. Campos, A. Jorio, and L. M. Malard, *Nano Letters* **17**, 3447 (2017), <https://doi.org/10.1021/acs.nanolett.7b00329>.

[50] L. Lange, K. Wang, S. Bange, L. Lafeta, B. Rosa, S. Reitzenstein, J. M. Lupton, and A. Hartschuh, *ACS Photonics* **11**, 3112 (2024), <https://doi.org/10.1021/acsphotonics.4c00388>.

[51] X. Wen, Z. Gong, and D. Li, *InfoMat* **1**, 317 (2019), <https://onlinelibrary.wiley.com/doi/pdf/10.1002/inf2.12024>.

[52] A. Autere, H. Jussila, Y. Dai, Y. Wang, H. Lipsanen, and Z. Sun, *Adv. Mater.* **30**, 1705963 (2018).

[53] M. S. Mrudul and G. Dixit, *Physical Review B* **103**, 10.1103/physrevb.103.094308 (2021).

[54] W. Mao, A. Rubio, and S. A. Sato, *Physical Review B* **109**, 10.1103/physrevb.109.045421 (2024).

[55] S. A. Mikhailov, *Physical Review B* **90**, 10.1103/physrevb.90.241301 (2014).

[56] H. A. Hafez, S. Kovalev, J.-C. Deinert, Z. Mics, B. Green, N. Awari, M. Chen, S. Germanskii, U. Lehnert, J. Teichert, Z. Wang, K.-J. Tielrooij, Z. Liu, Z. Chen, A. Narita, K. Müllen, M. Bonn, M. Gensch, and D. Turchinovich, *Nature* **561**, 507–511 (2018).

[57] K.-J. Tielrooij, A. Principi, D. S. Reig, A. Block, S. Varghese, S. Schreyeck, K. Brunner, G. Karczewski, I. Ilyakov, O. Ponomaryov, T. V. A. G. de Oliveira, M. Chen, J.-C. Deinert, C. G. Carbonell, S. O. Valenzuela, L. W. Molenkamp, T. Kiessling, G. V. Astakhov, and S. Kovalev, *Light: Science and Applications* **11**, 10.1038/s41377-022-01008-y (2022).

[58] G. Soavi, G. Wang, H. Rostami, D. G. Purdie, D. De Fazio, T. Ma, B. Luo, J. Wang, A. K. Ott, D. Yoon, S. A. Bourelle, J. E. Muench, I. Goykhman, S. Dal Conte, M. Celebrano, A. Tomadin, M. Polini, G. Cerullo, and A. C. Ferrari, *Nature Nanotechnology* **13**, 583–588 (2018).

[59] L. Wu, M. Brahlek, R. Valdés Aguilar, A. V. Stier, C. M. Morris, Y. Lubashevsky, L. S. Bilbro, N. Bansal, S. Oh, and N. P. Armitage, *Nature Physics* **9**, 410–414 (2013).

[60] L. Braun, G. Mussler, A. Hruban, M. Konczykowski, T. Schumann, M. Wolf, M. Münzenberg, L. Perfetti, and T. Kampfrath, *Nature Communications* **7**, 10.1038/ncomms13259 (2016).

[61] J. Pettine, P. Padmanabhan, N. Sirica, R. P. Prasankumar, A. J. Taylor, and H.-T. Chen, *Light: Science and Applications* **12**, 10.1038/s41377-023-01163-w (2023).

[62] A. Avdoshkin, V. Kozii, and J. E. Moore, *Phys. Rev. Lett.* **124**, 196603 (2020).

[63] D. E. Parker, T. Morimoto, J. Orenstein, and J. E. Moore, *Phys. Rev. B* **99**, 045121 (2019).

[64] J. Orenstein and J. S. Dodge, *Phys. Rev. B* **92**, 134507 (2015).